

All-in-one wearable drug efficacy assessment systems for bulbar muscle function using amyotrophic lateral sclerosis animal models

Received: 17 May 2024

Accepted: 5 August 2024

Published online: 09 August 2024



Beomjune Shin^{1,2,8}, Youngjin Kwon^{1,3,8}, Michelle Mittaz⁴, Hojoong Kim^{1,2}, Xiaoxing Xu⁴, Eugene Kim^{1,2}, Yoon Jae Lee^{1,5}, Jimin Lee^{1,2}, Woon-Hong Yeo^{1,2,6,7}✉ & Hyojung J. Choo⁴✉

Preclinical studies are crucial for developing amyotrophic lateral sclerosis drugs. Current FDA-approved drugs have been created by monitoring limb muscle function and histological analysis of amyotrophic lateral sclerosis model animals. Drug candidates for this disease have yet to be tested for bulbar-onset type due to the limitations of traditional preclinical tools: excessive animal use and discrete detection of disease progress. Here, our study introduces an all-in-one, wireless, integrated wearable system for facilitating continuous drug efficacy assessment of dysphagia-related muscles in animals during natural eating behaviors. By incorporating a kirigami-based strain-isolation mechanism, this device mounted on the skin of animals mitigates electromyography signal contamination caused by unpredictable animal movements. Our findings indicate this system, measuring the progression of motor neuron denervation, offers high precision in monitoring drug effects on dysphagia-responsible bulbar muscles. This study paves the way for more humane and efficient approaches to developing treatment solutions for degenerative neuromuscular diseases.

Amyotrophic lateral sclerosis (ALS), known as Lou Gehrig's disease, is a disease where motor neurons in the brain and spinal cord are selectively and gradually lost, leading to muscle weakness and eventually resulting in total paralysis¹. When ALS occurs, symptoms may begin with damage to lower motor neurons in the spinal region, causing weakness in the arms and legs, or with damage to motor neurons in the bulbar cord affecting the brain stem or spinal cord, leading to difficulties in swallowing and breathing^{2,3}. At the time of diagnosis, approximately 30% of ALS patients exhibit bulbar symptoms, and 70% of ALS patients with spinal symptoms⁴. Although the first 2 years of

spinal onset ALS patients do not present bulbar symptoms, most ALS patients will suffer from bulbar symptoms eventually^{5–7}. This progression makes voluntary movements such as walking, talking, and swallowing impossible, and the disease eventually leads to death when the diaphragm, a muscle involved in breathing, ceases to function. Most individuals with this disease remain mentally and sensory aware, having to endure the significant distress of watching their bodies become increasingly paralyzed. In the United States alone, about 5000 people are diagnosed with ALS each year, but approximately half of them die within three years of diagnosis, leaving around 30,000

¹Wearable Intelligent Systems and Healthcare Center (WISH Center) at the Institute for Matter and Systems, Georgia Institute of Technology, Atlanta, GA 30332, USA. ²George W. Woodruff School of Mechanical Engineering, Georgia Institute of Technology, Atlanta, GA 30332, USA. ³School of Materials Science and Engineering, Georgia Institute of Technology, Atlanta, GA 30332, USA. ⁴Department of Cell Biology, School of Medicine, Emory University, Atlanta, GA 30322, USA. ⁵School of Electrical and Computer Engineering, Georgia Institute of Technology, Atlanta, GA 30332, USA. ⁶Wallace H. Coulter Department of Biomedical Engineering, Georgia Institute of Technology and Emory University School of Medicine, Atlanta, GA 30332, USA. ⁷Parker H. Petit Institute for Bioengineering and Biosciences, Georgia Institute of Technology, Atlanta, GA 30332, USA. ⁸These authors contributed equally: Beomjune Shin, Youngjin Kwon. ✉ e-mail: whyao@gatech.edu; hyojung.choo@emory.edu

patients alive⁸. Despite this, the cause of the disease remains largely unknown. Currently, several drugs, including Riluzole (approved 1995), Nuedexta (approved 2011), Edaravone (approved 2017), Sodium Phenylbutyrate/Tauroursodiol (approved 2022), and Tofersen (approved 2023) have received FDA approval for slowing down the symptoms of the disease, and while there are various efforts aimed at treatment^{9,10}, a fundamental cure for the disease has yet to be discovered. Therefore, there is a significant investment in developing drugs to overcome this disease. In the process of creating new medicines related to ALS, rat models carrying the *SOD*^{G93A} mutation, which show symptoms and progression paths similar to human ALS, are often used^{11–13}. The efficacy of the developed drug can be assessed by monitoring the progression of the disease in the rodent model through various methodologies, including tracking changes in body weight^{12,14} and gait characteristics^{14–16}, assessing neuronal damage^{13,14,17–19}, and evaluating limb motor function²⁰. However, these conventional methods can analyze symptoms starting in the spinal region but have limitations in evaluating the bulbar region, resulting in omitted bulbar function tests in preclinical studies to assess Edaravone^{21–23}. However, symptoms that are initiated in the bulbar region progress rapidly and can lead to respiratory failure, or dysphagia-induced malnutrition, making them more life-threatening and emphasizing the importance of monitoring this region. Additionally, most methods capable of directly observing the deterioration of muscle function are invasive. This makes it challenging to observe without interfering with the natural behaviors of animals²⁴. Also, these methods induce permanent damage, limiting the measurement to be conducted only at the terminal stage, which makes continuous monitoring unavailable.

To address these issues, we introduce a drug efficacy assessment tool designed for animal studies, leveraging wearable electronics. This system facilitates the non-invasive monitoring of electromyography (EMG) signals from the masseter and digastric muscles, enabling the observation of muscle activity degradation due to ALS in the bulbar cord. In particular, we applied a kirigami pattern, which allows the adjustment of mechanical properties using incision patterns, to the device. The application of the kirigami pattern easily enhances the flexibility of substrates, leading to increased attempts to apply it to wearable devices recently^{25–27}. However, the use of these characteristics of kirigami has been limited to merely improving the conformality of the device. In contrast, we sophisticatedly designed the kirigami pattern to control the strain applied to the device, thereby implementing a kirigami-based strain isolator. This mitigates changes in the contact state between the electrodes and the skin caused by the rat's unintended movements, minimizing noise and ensuring high-quality signals. This approach, distinct from previously introduced strain isolation mechanisms in wearable devices²⁸, simplifies the process by merely perforating the substrate with a specific pattern, thereby maintaining high signal quality without complicating the system. The optimal strain-isolation design, derived through experimental and theoretical analysis with a model system, was implemented in the device. This device was utilized to monitor ALS progression in a rat model and to evaluate the effect of Edaravone on bulbar muscle denervation by tracking changes in the weekly muscle activity of chewing and swallowing-related muscles from onset to late stage. The reliability of the device in assessing drug efficacy was confirmed by comparing and validating the changes in muscle activity tracked by the device with the extent of muscle degradation assessed through the neuromuscular junction (NMJ) imaging analysis. This device establishes the foundation for a non-invasive, highly accurate assessment tool suitable for preclinical drug screenings that require continuous muscle activity monitoring. It is expected to significantly reduce the time and cost compared to traditional preclinical methods in the drug development process. Furthermore, this method is anticipated to enhance the efficacy of translational medicine in the bulbar region, an area often challenged by signal quality due to frequent movements.

Results

Design, architecture, and drug efficacy assessment procedure of a wearable electronic system

Figure 1A shows an overview of the system tailored for drug efficacy assessment in animal models. This device consists of two electrode patches for measuring EMG signals induced during swallowing motions, a circuit for processing and transmitting data, and an interconnector linking these components. The electrodes are attached to the skin of the jaw and cheek of the rat, respectively, to monitor the EMG signals generated when the rat eats the food. The electrodes are arranged in alignment with the direction of the muscle fiber to measure the potential difference generated by each muscle group. The measured EMG signal is wirelessly transmitted through the circuit, and data is collected via a mobile device (Supplementary video S1). This system is seamlessly mounted on the body of rats, measuring, and recording muscle activity related to eating. Muscle activity was measured weekly, and the trend of the change in muscle activity was tracked and compared among three distinct rat cohorts, consisting of wild-type (healthy control), ALS model, and ALS model with ALS drug treatment. By comparing the relative muscle activity degradation trends between groups, the ALS symptomatic progress and effectiveness of the administered drug on ALS can be non-invasively quantified. In ALS model rats, muscle activity diminishes due to the denervation and death of motor neurons, which results in weakened or severed connections between these neurons and muscle cells (Fig. 1B). We conducted experiments by administering Edaravone, an FDA-approved drug known to delay denervation in ALS patients, to the drug-treated group. Specifically, to monitor symptoms of chewing and swallowing difficulty due to denervation, electrode patches were placed to measure the EMG signals of the masseter and digastric muscle groups innervated by the bulbar cord, as depicted in Fig. 1C. Animal experiments have certain limitations that need to be addressed. These limitations include changes in signal quality due to the movement of the electrode on the skin, the risk of detachment of the device due to movement, and resistance changes caused by the deformation of the interconnector. To mitigate these issues, the device was designed to minimize these limitations, as illustrated in Fig. 1D. To prevent the circuit from being scratched on the ground or detached by the rat itself due to its movements, the circuit with a rechargeable battery was positioned on the back of the rat. The battery lifetime tests appear in Fig. S1. The interconnector, which interfaces between the circuit and electrodes, was designed in a zigzag shape to easily stretch with the movements of rats without detaching from the body. A sandwich structure was created using a copper serpentine interconnector and an interlayer made up of silicone, acting as an insulator to ensure maximum adhesion while connecting the electrodes and circuit within a confined space (Fig. S2). The interconnector featuring the zigzag shape with sandwiched wires exhibits an adhesion strength about 4 times higher than an interconnector without a sandwich structure and zigzag pattern in the same area (Fig. S3). Moreover, a kirigami pattern was applied to the electrode patch to minimize changes in the contact state between the electrode and the skin that could occur due to jaw movements while the rat chews. This design effectively prevents the propagation of strain to the electrode. By applying these elements, the device was seamlessly attached to the body of the rat, as shown in Fig. 1E. Despite the vigorous movements of rats, this device did not fall off, and it was possible to measure high-quality signals with minimized motion artifacts.

Theoretical background for the mechanical design of the strain-isolation mechanism

The modality, sEMG, used for tracking muscle activity in drug efficacy assessment in the ALS rat model inherently has the potential to be contaminated by some noise sources. The change in contact state between the skin and the electrode is a typical noise source²⁹.

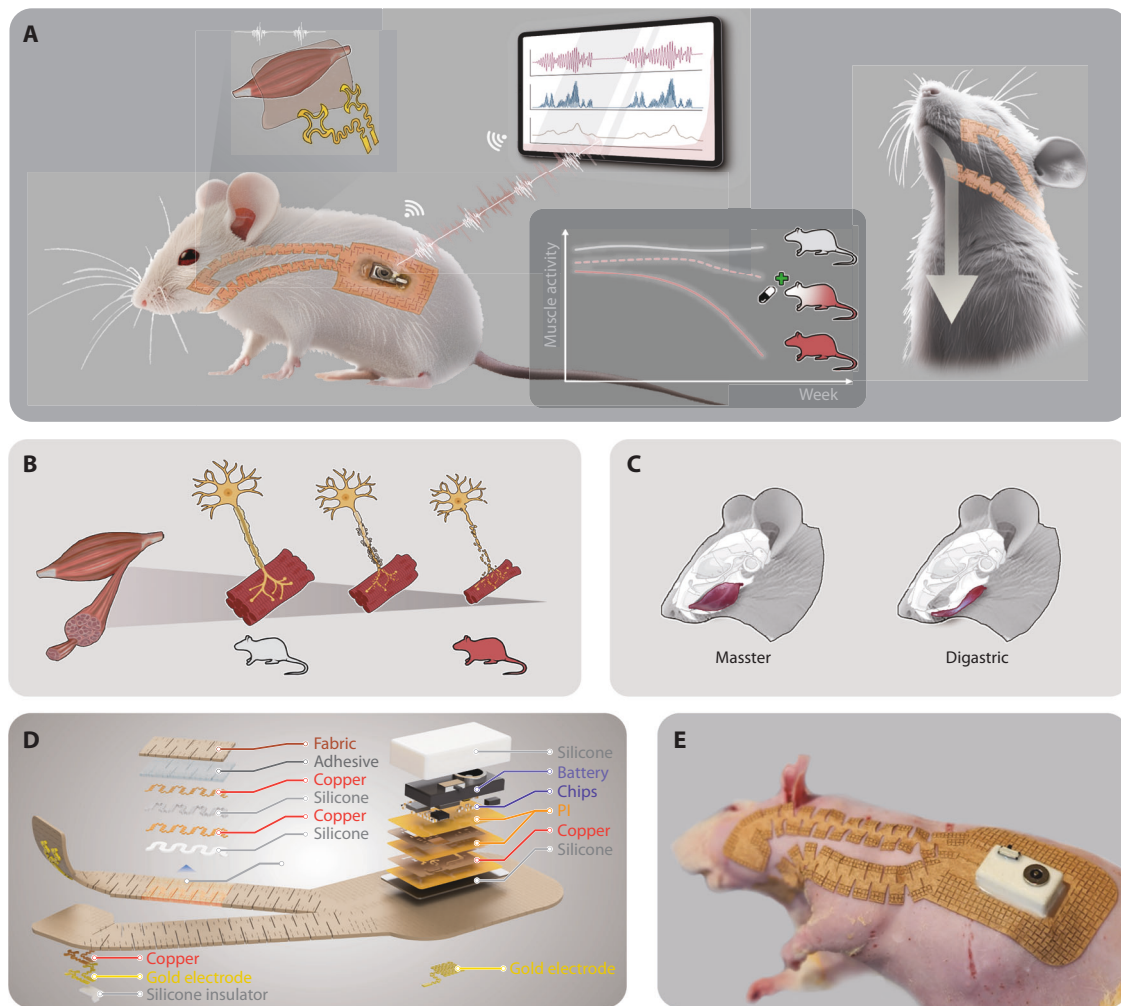


Fig. 1 | Design, architecture, and the process of assessing drug efficacy using an all-in-one, wireless, integrated wearable drug efficacy assessment system. A An illustration of the process for evaluating drug efficacy using a wearable device optimized for animal experiments (left), featuring a kirigami strain-isolation mechanism of the wearable electrode (right). **B** Schematic anatomy of the head of a rat, showing the location of muscles playing pivotal roles in swallowing. **C** A

schematic illustration of the progression of motor neuron denervation associated with the advancement of ALS. **D** Exploded views of the integrated wearable system, including two EMG electrodes enhanced by the perforated electrode patch, a zigzag-shaped sandwich interconnector, and a wireless circuit. **E** A photograph of the ultrathin wearable system seamlessly mounted on the rat. Scale bar: 10 mm.

Especially when measuring sEMG using dry electrodes, changes in the contact state between the skin and the electrodes critically affect the recorded signal. When the skin in contact with the electrode is stationary, the electrode can maintain conformal contact due to the conformity of the elastomeric layer directly bonded to the electrode. However, the movement in the skin, like when rats eat food, induces relative motion between the skin and the electrode by the difference in modulus between the electrode and the elastomeric layer. Consequently, the skin-electrode interface constantly changes, altering skin impedance and affecting the signal. A kirigami strain-isolation mechanism was applied to address the issue of maintaining consistent contact between the electrode and skin during movement. This approach allows for the exploitation of the benefits of dry electrodes, which include being hypoallergenic to the skin, ease of use, and reusability³⁰. As a result, consistent contact between the electrode and the skin was ensured even when the skin with the attached electrode moved significantly. The electrode patch of the device consists of a serpentine-structured gold nano-membrane-based dry electrode transferred onto a patch made of polyurethane non-woven fabric and silicone adhesive. The biocompatibility study results of materials

consisting of the device appear in Fig.S4. The edges of the fabric patch, where the electrodes are not placed, were perforated with a biaxial kirigami pattern to be utilized as a strain isolation band (Fig. 2A). As shown in Fig. 2B, the design of the biaxial kirigami pattern is defined based on the dimensions of the unit cell. The unit cell is a square shape with a length of $2L$ on each side, and perforations are made in horizontal and vertical directions to create a gap, δ . A kirigami-patterned sheet with these unit cells demonstrates the properties of an auxetic material with a negative Poisson's ratio when strain is applied, as the cut corners rotate, as depicted in Fig. 2C. Moreover, thanks to the increased degree of deformation allowed by the kirigami pattern, the sheet perforated with the kirigami pattern is subjected to smaller stress under the same strain than a plane sheet. This can be represented as having a lower effective Young's modulus, E_{eff} , which has the following relationship with δ and L , which are the critical determinants of the biaxial pattern³¹.

$$E_{\text{eff}} = \frac{2}{3} E \left(\frac{\delta}{L} \right)^2 \quad (1)$$

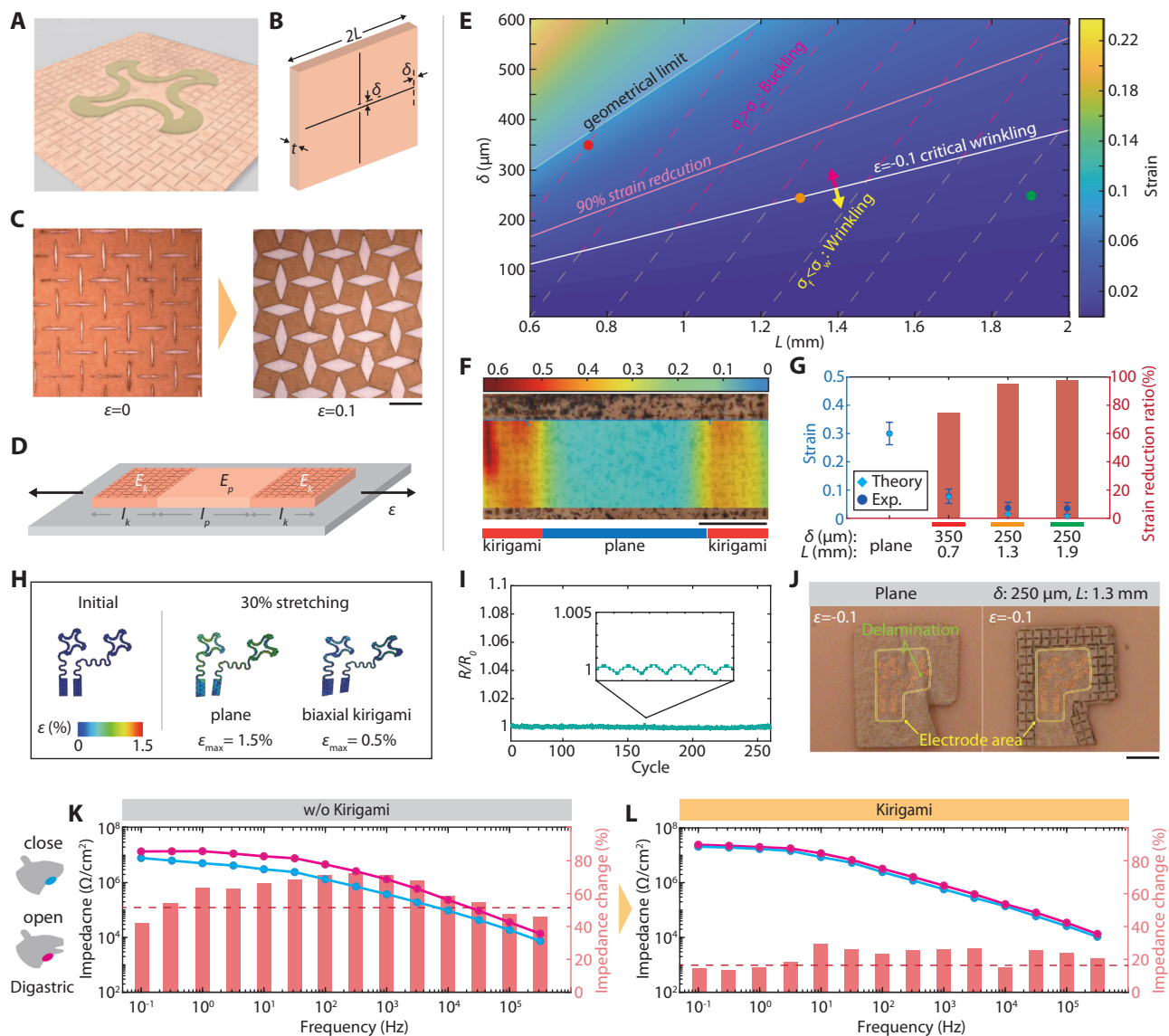


Fig. 2 | Design and characterization of strain-isolation systems. **A** An illustration of a single-unit design of an electrode integrated into the kirigami-patterned adhesive layer. **B** A detailed scale of the unit cell of the biaxial kirigami pattern. **C** Deformation results of a kirigami pattern at 10 percent biaxial strain, showing elongation accompanied by rotation at the ends of the perforated lines. Scale bar: 2 mm. **D** A multi-electrode patch design with perforations at both ends. **E** Contour map of strain at the midpoint of the patch where the electrode is located, determined by the factors δ and L in the biaxial pattern. **F** Strain distribution outcomes across different parts of the patch, visualized through DIC. Scale bar: 5 mm. **G** Comparison results between theoretically predicted strain and experimentally measured values at the center of the patch, along with the strain reduction ratio. **H** FEA results showing the maximum biaxial strain on the electrode integrated into the patch. **I** Experimental results showing the measured electrical resistance of the electrode under cyclic loading of 30% biaxial strain, showing negligible changes. **J** Comparison photos of a plain patch (left) and a kirigami patch (right) designed to prevent buckling delamination. The plain one shows delamination at the electrode location, whereas the kirigami one maintains the surface conformal contact. Scale bar: 5 mm. Measured impedance changes at the digastric muscle during mouth closing (blue points) and opening (red points) motions, without kirigami (**K**) and with kirigami (**L**) patterns applied to the patch, respectively.

When the modulus of a substrate is configured to vary in specific areas, the distribution of strain applied to it is determined by the configuration of the modulus³². We achieved an effect of strain isolation and alleviated buckling delamination by perforating a kirigami pattern at both ends of a fabric patch, thereby patterning the modulus on the substrate. To find a design that could optimize these performances, we used a model system for parametric analysis. As shown in Fig. 2D, the model was prepared by perforating both ends of a plane patch with biaxial patterns of various dimensions. The perforated and plane parts are characterized by lengths l_k and l_p , and Young's moduli E_k and E_p , respectively. The total effective Young's modulus of the patch, E_{tot} , is expressed as $E_{\text{tot}} = \Sigma l_i (\Sigma l_i E_i)^{-1}$, where l_i and E_i represent

Data are presented as mean values with the standard deviation of the mean of 5 experimental values each. **H** FEA results showing the maximum biaxial strain on the electrode integrated into the patch. **I** Experimental results showing the measured electrical resistance of the electrode under cyclic loading of 30% biaxial strain, showing negligible changes. **J** Comparison photos of a plain patch (left) and a kirigami patch (right) designed to prevent buckling delamination. The plain one shows delamination at the electrode location, whereas the kirigami one maintains the surface conformal contact. Scale bar: 5 mm. Measured impedance changes at the digastric muscle during mouth closing (blue points) and opening (red points) motions, without kirigami (**K**) and with kirigami (**L**) patterns applied to the patch, respectively.

the length and Young's modulus of each part of the patch. When the model undergoes strain, ϵ^* , the strain applied to each part is expressed by the lengths and Young's moduli of each as $\epsilon_i = E_{\text{tot}} \epsilon^* / E_i$. As a result, when a model with l_k and l_p of 5 mm and 10 mm, respectively, undergoes 30% stretching ($\epsilon = 0.3$), the strain applied to the non-perforated section of the patch where the electrode is located is distributed according to the dimension of the biaxial kirigami pattern, as shown in Fig. 2E. The white shading in the contour map indicates the geometrical limit, $L < 2\delta$. The 90% Strain reduction line, indicated as pink, represents the boundary of dimensions that can achieve more than 90% strain reduction compared to the strain the model would receive without applying the kirigami pattern. When bonded layers of different

moduli are subjected to compression, delamination can occur at the interface³³. For a thin elastic layer, such as the patch bonded to a thick elastic substrate like skin, buckling instability is induced according to the deformation of the substrate. The critical stress for wrinkling is expressed as

$$\sigma_w = \frac{\bar{E}_f}{4} \left(\frac{3\bar{E}_s}{\bar{E}_f} \right)^{2/3}, \quad (2)$$

where \bar{E}_f and \bar{E}_s are the plane strain modulus of the elastic layer and the substrate, respectively³⁴. When the compressive stress in the elastic layer, σ_f , is less than σ_w , the layer deforms compliantly without causing delamination at the interlayer, leading to wrinkling. Therefore, the conformal contact of electrodes underneath the patch is maintained regardless of the motion. However, when $\sigma_f > \sigma_w$, spontaneous buckling occurs, forming a gap at the interface between the two layers. This induces unstable contact between the electrode and skin, and small movements can cause significant changes in contact impedance. In Fig. 2E, the critical wrinkle stress line, indicated by a white line at a strain of -0.1 , distinguishes between the upper region (red), where buckling delamination occurs, and the lower region (yellow), where wrinkling happens instead. The electrode patch design should be below the white line to maintain stable skin-electrode contact.

Experimental result of the strain-isolation mechanism applied electrode patch

To validate the computational results of the strain isolation effect achieved by applying the kirigami pattern, the actual strain applied to the specimen was visualized using the digital image correlation (DIC) method³⁵, as shown in Fig. 2F. (For detailed information, please see Supplementary Note 1, Fig. S5) The DIC measurements were conducted for samples marked in Fig. 2E with red (Case 1: $\delta = 350 \mu\text{m}$, $L = 0.7 \text{ mm}$), yellow (Case 2: $\delta = 250 \mu\text{m}$, $L = 1.3 \text{ mm}$), and green (Case 3: $\delta = 250 \mu\text{m}$, $L = 1.9 \text{ mm}$) dots, respectively. The experimental data (dark blue circles in Fig. 2G) correspond well with the trend of the calculated prediction (sky blue diamonds in Fig. 2G). For patches with kirigami patterns in cases 2 and 3, it was verified that they performed over 90% strain reduction under the same deformation conditions as a plane patch, acting as an effective strain isolation mechanism. As a result, when the patch is stretched by 30%, electrodes embedded beneath the patch in both plane patches and biaxial kirigami patterned patches exhibit maximum strains of 1.5% and 0.5%, respectively (Fig. 2H). The kirigami patch effectively suppresses the deformation of the electrode itself, showing only less than 0.1% resistance change in repeated 30% stretching experiments, as illustrated in Fig. 2I. Furthermore, our model revealed that the kirigami pattern effectively suppresses buckling delamination, as evidenced by the identified critical buckling boundary. This means that even when compression strain is applied to the patch, the area where the electrode is positioned remains in contact with the skin phantom, avoiding detachment, as shown in Fig. 2J. Therefore, the patch deforms conformally with the movement of the skin, simultaneously preventing relative movement at the interface between the electrode and the skin. The detailed experimental methods appear in Supplementary Note 2, Fig. S6. We have identified an optimal design configuration based on calculations and experimental results related to the strain isolation capabilities and resistance against buckling delamination the Kirigami pattern offers. While increasing δ and L contributes to a lower modulus, thereby improving the functional performance of the patch, it simultaneously leads to diminished stiffness. Reduction in stiffness complicates the handling of the patch and renders it unsuitable for repeated applications. Therefore, among designs that offer more than 90% strain reduction while preventing the occurrence of buckling delamination, we selected the design with δ and L to $250 \mu\text{m}$ and 1.3 mm , respectively, to ensure a high modulus for

achieving ease of reuse. Applying the kirigami pattern allows the patch to isolate strain and resist buckling delamination effectively. To verify its effectiveness on actual rats, the impedance of the electrode was measured as the rat opened and closed its mouth. By measuring the changes in impedance due to the difference in opening and closing the mouth under the same skin conditions and with the same electrode, effective observation of changes in the contact pattern between the electrode and skin was possible. When measured near the digastric, a plane patch without kirigami showed an average impedance change of about 50% upon opening and closing the mouth (Fig. 2K), whereas patches with a kirigami pattern showed an average change of about 17% (Fig. 2L). The results obtained from the measurement from the masseter also demonstrated a similar trend (Fig. S7). This indicates that the electrode patch with the kirigami pattern maintains constant contact between the electrode and skin despite the movements of the attached skin, enabling stable signal acquisition.

Enhanced motion artifact control in animal models through kirigami strain-isolation

We conducted a comparative experiment to validate the effects of the kirigami strain-isolation mechanism when applied to rats. A device designed to minimize the potential influences on the signal quality other than the electrode patches was prepared for comparison. As shown in Fig. 3A, the device connected two EMG sensors, one with an optimal kirigami pattern and the other plain, in a zigzag interconnector (under -0.1% resistance change under 30% stretching, Fig. S8) within a single circuit, thereby equally limiting potential noise-inducing factors aside from the contact between the electrode under the patch and the skin. The setup was designed so that each patch was placed to record the EMG signals from the other masseter muscle groups of the rat, specifically with the kirigami-patterned patch on the left side and the plane patch on the right side (Fig. 3B). Before attaching the electrodes, the skin was prepared through a procedure³⁶ to ensure consistent impedance levels. Rats continuously exhibit movements ranging from large actions, such as twisting their bodies or scratching their torsos with their front paws (Supplementary video S2), to smaller movements like sniffing or bruxing (Supplementary video S3). We normalized the sEMG signal values to the base noise level when the target muscles were at rest without movement. Even when the rat appears still, continuous small movements, such as sniffing, induce consistent noise in the plane patch, as shown in Fig. 3C. On the other hand, the kirigami patterned patch suppresses the relative movement between the electrode and skin, maintaining a constant contact state and effectively isolating such noise. Consequently, the kirigami patterned patch shows a root mean square (RMS) noise value of approximately 75% lower than the plane patch (Fig. 3D). Moreover, in situations where the rat is eating food, clear swallowing peaks in the EMG signal are detected with the kirigami patch, as illustrated in Fig. 3E. However, the signal acquired from the plain patch is obscured by significant noise. This implies the kirigami pattern helps to effectively capture small EMG signals from the masseter muscle group. As a result, the signal-to-noise ratio (SNR) of the EMG signals measured from the masseter muscle group during swallowing motions showed a significant difference between cases with and without applying the kirigami pattern, 12.1 dB and 4.6 dB, respectively (Fig. 3F).

Monitoring disease progression and evaluating drug efficacy in ALS rat model using EMG-based muscle activity tracking

An experiment was conducted using a wearable drug efficacy assessment tool on an ALS rat model to verify if the device could detect the effects of Edaravone. As shown in Fig. 4A, over an approximately 10-week period, we monitored and compared the trends in muscle activity changes across three groups of age and sex-matched rats. These groups were categorized as the healthy group (wild-type male rats), the ALS group (*SOD^{G93A}* male rats), and the ALS + Drug group

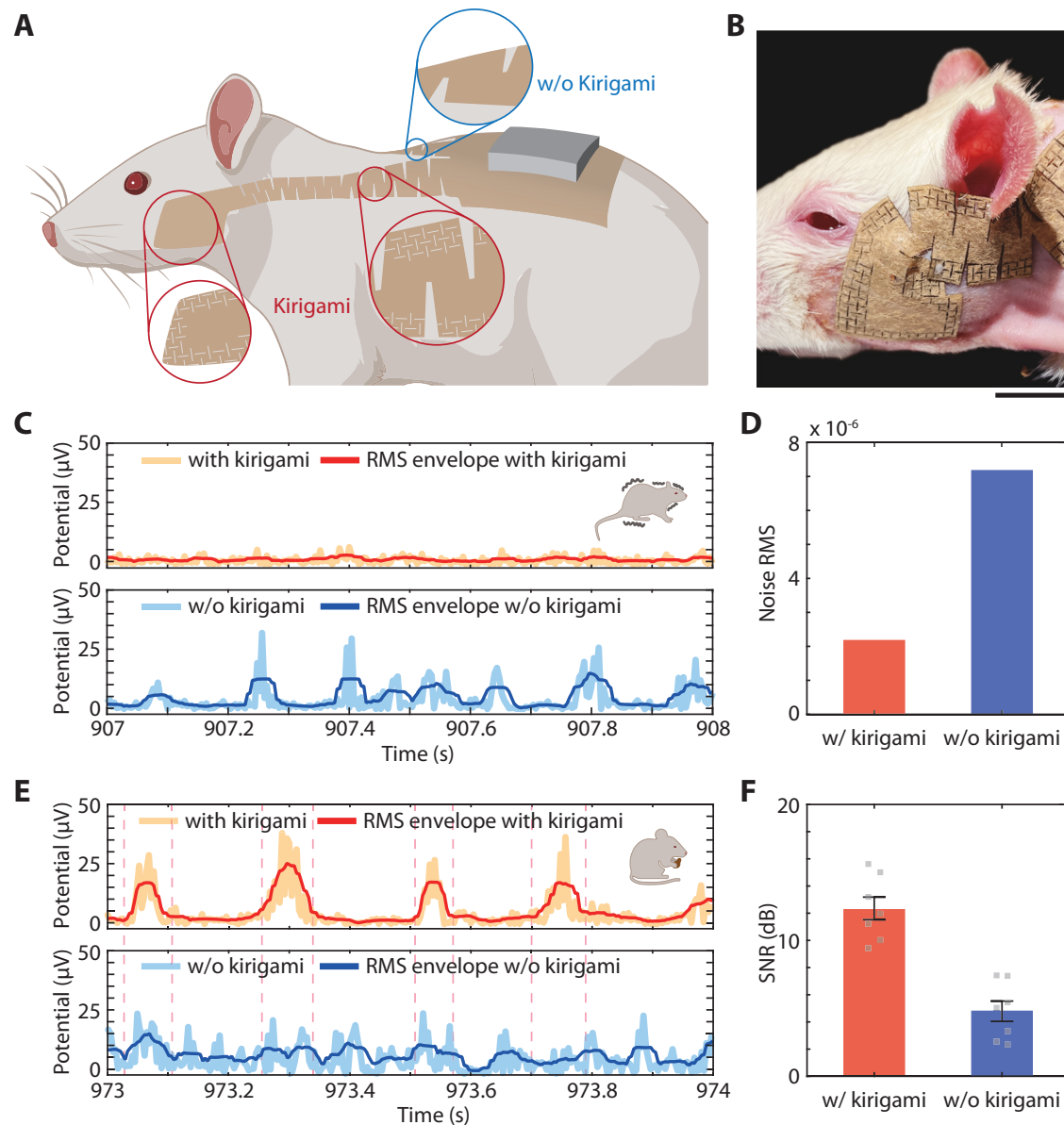


Fig. 3 | Enhanced signal quality by utilizing the strain-isolation mechanism on the electrode patch. **A** An illustration showing an experimental setup to validate the electrode's performance with the strain-isolation mechanism using kirigami patterns (Created with BioRender.com released under a Creative Commons Attribution-NonCommercial-NoDerivs 4.0 International license (<https://creativecommons.org/licenses/by-nc-nd/4.0/deed.en>)). **B** A photo of a kirigami-patterned electrode mounted on the masseter muscle area of the rat. Scale bar: 10 mm. **C** Comparison of measured EMG signals from two types of electrodes (top: with kirigami and bottom: without kirigami) when there is no movement in the

masseter region of the rat. Data presented with rectified EMG signal and the root mean square (RMS) envelope of it. **D** Summarized RMS values that measure baseline noise without a rat's motion in (**C**). The results show significant noise reduction by the strain-isolation due to the kirigami structure. **E** Comparison of measured EMG signals from two types of electrodes (top: with kirigami and bottom: without kirigami) when the rat eats food, generating swallowing motions. **F** Summarized SNR, demonstrating significantly higher signals from the kirigami electrode than the plain one. Data are presented as mean values with the standard error of the mean.

(Edaravone-treated *SOD*^{G93A} male rats). To specifically focus on the effects of the drug on ALS occurring in the bulbar cord, EMG signals from the masseter and digastric muscles were monitored during eating. Previous research findings show that the onset of ALS in the *SOD*^{G93A} model occurs between weeks 17 (spinal cord) and 19 (bulbar cord), so the monitoring commenced from week 18 for effective observation^{11–13,37}. The drug-treated group had an osmotic pump loaded with Edaravone implanted at week 20 to ensure a consistent supply of the drug. To maintain consistent skin conditions in rats affecting EMG signal accuracy, we prepped the skin with alcohol swabs before electrode attachment, ensuring similar impedance levels in a

motionless state (For a detailed preparation process for the experiment, please see Supplementary Note 3). Additionally, to reduce individual variability, the base noise—measured value from still, non-moving—served as a reference for normalizing the analysis signal. At week 18, when the monitoring was initiated, the ALS group rats had not yet shown any symptoms. Thus, as shown in Fig. 4B, C, significant peaks were observed in the normalized EMG amplitude in both the masseter and digastric muscles during eating, making them easily distinguishable in the signal. However, by week 26, as ALS symptoms had progressed, there was a noticeable decrease in the measured normalized EMG amplitude during swallowing (as shown in Fig. 4D, E).

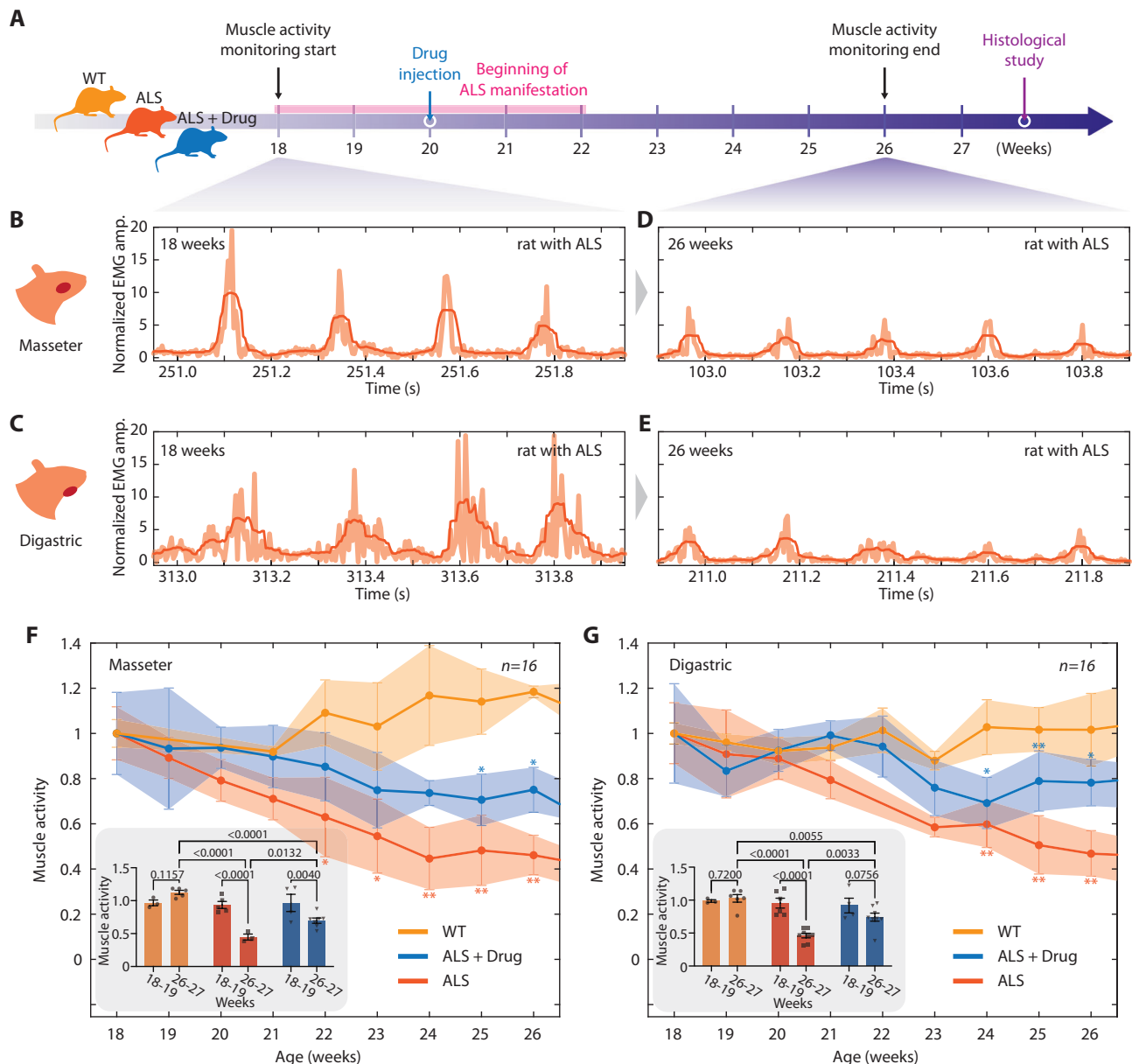


Fig. 4 | Drug efficacy assessments with rats. **A** An overview of a multi-week evaluation of drug efficacy with three types of models, including wild-type (WT), ALS group (ALS), and drug (Edaravone) treated ALS group (ALS + Drug). The sensor-enabled muscle activity monitoring starts at week 18. Measured swallowing EMG signals which are presented by normalized EMG amplitude of the ALS group rats (*SOD^{93A}*) at the **(B)** masseter and **(C)** digastric muscle areas, respectively, at week 18, before ALS manifestation. **D, E** Measured swallowing EMG signals from the same group in **(B, C)** at week 26 after ALS manifestation, showing significant reduction of muscle activities. Normalized muscle activity changes from three groups, including WT ($n = 6$), ALS ($n = 4$), and ALS + Drug ($n = 6$) at the **(F)** masseter **(G)** digastric muscle areas, capturing that the signals of the ALS+Drug group are a lot higher than the ALS group. The results indicate a clear therapeutic effect of the drug (Edaravone) on delaying bulbar muscle activity decline. Data are presented as

mean values with the standard error of the mean. Two-way ANOVA with Tukey's multiple comparison test analyzes these data; * $p < 0.05$ and ** $p < 0.01$ compared to wild-type. For digastric muscles, p -values comparing WT vs ALS at 24, 25, and 26 weeks are 0.01, <0.0001, and <0.0001, respectively. p -values comparing WT vs ALS+Drug at 24, 25, and 26 weeks are 0.0103, 0.0095, and 0.0108, respectively. For masseter muscles, p -values comparing WT vs ALS at 22, 23, 24, 25, and 26 weeks are 0.0108, 0.0239, 0.0006, 0.0003, and 0.0006, respectively. p -values comparing WT vs ALS+Drug at 25, and 26 weeks are 0.0272 and 0.0193, respectively. The inset graphs in **(F, G)** represent the comparison of muscle activity of each group between weeks 18-19 and weeks 26-27. The individual dot indicates data from each animal on each week. P -values are presented on the tip of comparison pairs. Data are presented as mean values with the standard error of the mean.

In contrast, in the wild-type group, no significant changes were observed between weeks 18 and 26. EMG signal values measured weekly from weeks 18 to 26 were translated into muscle activity levels and plotted for the masseter and digastric muscles (Fig. 4F, G). Muscle activity represents the degree of change relative to the normalized EMG amplitude at week 18 for each group. In the case of the wild-type, digastric and masseter muscle activity at week 26 did not decrease

noticeably and tended to remain stable or even increase compared to week 18. This is attributed to muscle development as the experiment was conducted throughout continuous growth for the rats. On the other hand, the ALS group showed a significant decrease in muscle activity over time. The activities of the masseter and digastric muscles showed a significant decrease starting from week 22 and week 24, respectively. In the drug-treated group, masseter and digastric muscle

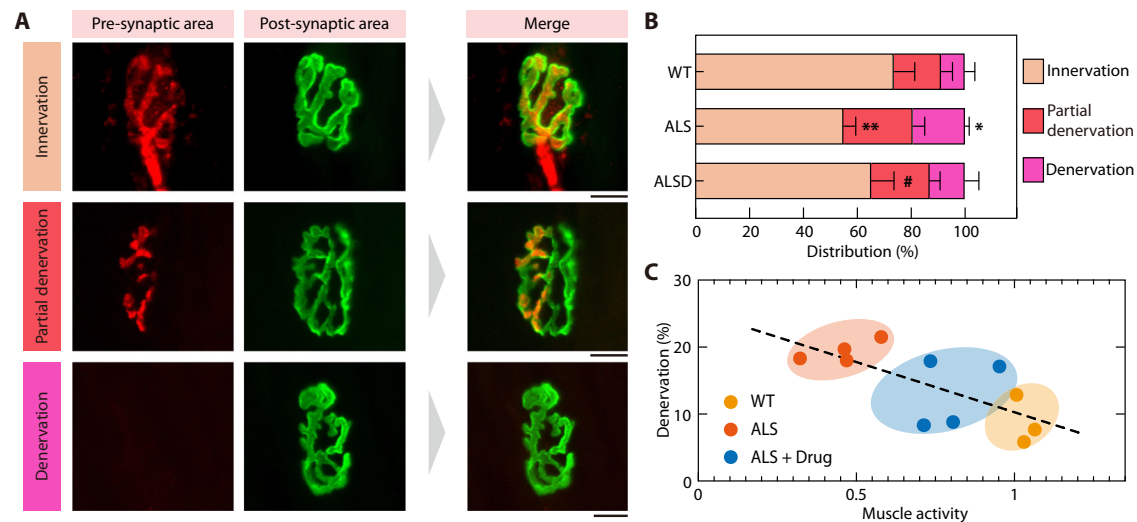


Fig. 5 | Verification of EMG-based muscle activity with NMJ analysis in ALS model rats. **A** Representative images of innervated, partially innervated, or denervated NMJs. Pre-synaptic terminals (red fluorescent image) were stained with anti-neurofilament and anti-synaptic vesicle antibodies, and post-synaptic terminals were probed with FITC-conjugated α -bungarotoxin. Scale bar: 10 μ m. More than 100 NMJs were analyzed from each muscle of each animal. **B** The innervation status of NMJs (>100 NMJs) in digastric muscles at 28 weeks old of each group was

analyzed. $N = 3$ for WT and $n = 4$ for ALS or ALSD group. Data were analyzed using two-way ANOVA with Tukey's multiple comparison test. " indicates $p = 0.002$ (WT vs ALS in innervation), " indicates $p = 0.0351$ (WT vs ALS in denervation), and # indicates $p = 0.0251$ (ALS vs ALSD in innervation). Error bars indicate the standard error of the mean. **C** Correlation between denervation rates at 28 weeks old and muscle activity at 27 weeks old of digastric muscles. Each dot indicates an individual rat in the group.

activities were decreased later or less than the ALS group. The muscle activity for each group was compared between weeks 18–19 and weeks 26–27 to confirm significant differences between the groups, as shown in the inset graphs in Fig. 4F, G. These results confirm that masseter and digastric muscle activities of drug-treated ALS groups are significantly lower than WT groups, but higher than ALS groups at weeks 26–27 indicating the therapeutic effect of Edaravone on delaying bulbar muscle activity decline.

Verification of EMG-based muscle activity with NMJ analysis in ALS model rats

After completing 9 weeks of EMG signal measurements, the decrease in muscle activity was compared and verified against the extent of muscle denervation determined through the NMJ analysis. To investigate the protective effect of Edaravone on the neuromuscular connection of bulbar muscles, we examined the status of NMJ of digastric muscles. The pre-synaptic area was stained with neurofilament and synaptic vesicles, and the post-synaptic area was stained with α -bungarotoxin to label acetylcholine receptors on the surface of the muscle (Fig. 5A). By quantification of more than 100 NMJs in the digastric muscles of each rat per group, the ALS group presented significantly lower innervated NMJs but higher denervated NMJs compared to the wild-type group, as expected. Edaravone increased innervated NMJs in SOD^{G93A} rats compared to vehicle-treated SOD^{G93A} rats statistically ($p < 0.05$) and decreased the trend of denervated NMJs ($p = 0.1$) (Fig. 5B). Although NMJ status was distinguished between groups, daily food, and water consumption were not different between wild-type and ALS groups (Fig. S9). Lastly, we confirmed the negative correlation between surface EMG amplitude and denervation rates by NMJ analysis (Fig. 5C), which validates the measurement of surface EMG as a reliable tool to monitor the innervation/denervation of skeletal muscles for disease progress or functional recovery by treatment.

Discussion

This paper reports a wireless integrated wearable platform for assessing drug efficacy on bulbar muscle function using an ALS rat model. Unlike traditional drug testing methods, this non-invasive

system can offer real-time, wireless, continuous monitoring of bulbar muscle function, allowing the experiment to be conducted with natural eating behavior. The kirigami strain isolation mechanism secures the consistent skin contact status of the electrode during the rat's feeding. This feature suppresses noise generated by unintended movements and the rapid jaw and neck movements when the rats chew and swallow, thus allowing for higher-quality signal measurement. Continuous monitoring of the bulbar muscle EMG signals of ALS rats using the wearable systems detects a decline in bulbar muscle activity, confirmed by histological analysis of NMJ denervation. This result demonstrates that our system can effectively capture the denervation delay effect of the drug, facilitating a highly reliable, non-invasive monitoring of ALS progression in the bulbar cord. The wearable system establishes the foundation for a non-invasive, highly accurate assessment suitable for more effectively conducting preclinical studies by assessing various muscles in different locations across numerous animal models. In addition, this system can successfully detect ALS symptomatic progression and the efficacy of the drug to delay functional decline statistically, with a relatively small number of animals indicating sensitive and reproducible measurements. Therefore, we expect this device will significantly reduce the time and cost compared to the traditional preclinical drug development process. Furthermore, this method is anticipated to enhance the efficacy of translational medicine in the bulbar region, an area that often faces challenges with signal quality due to frequent movements.

Methods

Wearable device design

Various electronic components were incorporated to design the wearable drug efficacy assessment tool for animal models. Alongside the standard passive elements like resistors, capacitors, and inductors, the circuitry also integrated the BLE SoC (nRF52832, Nordic Semiconductor). ADS1292 Analog-Front-End chips from Texas Instruments were utilized to capture signals from each electrode for measuring masseter and digastric (Fig. S10). As depicted in Fig. S11, the system is configured to transmit raw signals measured from two electrodes

through a comprehensive filtering process to a mobile device. This process includes pre-processing, band-pass filtering (BPF) to retain the relevant EMG frequency range, notch filtering to eliminate specific noise frequencies, and quality assessment to ensure signal integrity. Post initial processing, the signals are converted into digital signals by an Analog-to-Digital Converter (ADC), and digital data is then transmitted to a Microcontroller Unit (MCU) via SPI (Serial Peripheral Interface) communication protocol. Following reconstruction, the processed and filtered EMG digital signals are wirelessly transmitted to a remote tablet using Bluetooth Low Energy (BLE), established with a communication protocol (Nordic SoftDevice). Custom mobile application developed with Kotlin-based, Android native environment received signals with real-time continuous stream buffer and decoded to readable decimal format, integrated with timestamp data. An Infinite Impulse Response (IIR) filter is implemented on the mobile application for further noise reduction and signal enhancement. This two-stage filtering approach significantly improves the SNR and data reliability, enabling real-time analysis of muscle activity during rodent feeding.

Experiment design for drug efficacy test

SOD^{G93A} male rats (Taconic Biosciences) were randomly selected and assigned to vehicle-treated ($n = 4$) or Edaravone-treated groups ($n = 6$). Wild-type male rats ($n = 6$) were used as healthy controls. Due to the earlier onset and accelerated disease progress of male *SOD^{G93A}* rats compared to female ones³⁸, we only used male rats in this study. When rats were 18 weeks old, body weight was monitored three times per week, and EMG of the masseter and digastric muscles were measured while eating a rodent chew once a week as outcomes. To motivate food consumption, rats were subjected to 16 h starvation before EMG measurement. At 20 weeks old, an Edaravone- or vehicle-contained osmotic pump was inserted subcutaneously in *SOD^{G93A}* male rats for continuous drug release for 8 weeks by replacing osmotic pumps every 2 weeks three times. The muscle activity was extracted from the measured EMG signal of each week and analyzed by two-way ANOVA with Tukey's multiple comparison test to determine differences between groups from 18 weeks old to 27 weeks old. At 28 weeks old, all rats were euthanized, and the digastric muscles were isolated for NMJ analysis. The proportion of denervated NMJs among the analyzed NMJs was used to evaluate the muscle activities of each muscle as the final endpoint.

Osmotic pump implant for drug delivery

For all animal surgeries, the proper aseptic technique was used, and all drapes, supplies, surgery tools, and gloves were sterilized. *SOD^{G93A}* rats (20 weeks old) were anesthetized with 2–3% isoflurane and given a subcutaneous injection of buprenorphine (0.1 mg/kg) to minimize pain post-surgery. Hair on the right side of the back, slightly posterior to the scapulae, is shaved and removed with Nair, and the skin is prepared by three alternative wipes of Prevacis swabs (combination of chlorhexidine and alcohol wipes, PDI) and 70% ethanol (in water). Osmotic Pumps (Alzet, 2 ml for 14-day release) were filled with 125 mg of Edaravone (Cat no. 443300, Sigma Aldrich) in 2 ml of 25% Ethanol/saline to provide drug delivery 15 mg/kg/day^{23,39}. The incision was made for osmotic pump placement, and a hemostat was inserted into the incision, creating a subcutaneous pocket through open and close movement. The drug/vehicle-filled pump was placed into the subcutaneous pocket, and the incision was closed with wound clips. Animals with surgery and surgery sites were monitored for 3 days. Osmotic Pumps were replaced every 2 weeks 3 times.

Immunohistochemistry and immunofluorescence

Commonly used procedures have been adopted to perform NMJ analysis for muscle denervation⁴⁰. Muscle sections were permeabilized

with 4% Triton-X and blocked for 90 min and blocked with 4% bovine serum albumin (BSA) and 2% Triton-X (blocking buffer) for 30 min. Subsequently, primary antibodies for presynaptic terminal detection by combining 2H3 (anti-neurofilament antibody, 1:50, DSHB) and SV2 (anti-synaptic vesicles antibody, 1:50, DSHB) were prepared in blocking buffer and incubated muscle sections for 3 days at 4 °C. After washing sections 4 times with washing buffer (0.2% Tween-20 in PBS) and sections were incubated with Alexa Fluor 488-conjugated secondary antibodies (Donkey anti-mouse IgG, Jackson ImmunoResearch) overnight at 4 °C followed by 4 times washing. Acetylcholine receptors, postsynaptic terminal proteins, were stained with α -bungarotoxin conjugated with tetramethylrhodamine (Sigma Aldrich) 1 μ g/mL for 30 min. Before imaging, the slides with stained sections were mounted with Vectashield (Vector Labs).

NMJ denervation analysis

Z-stack images of 30 μ m thick longitudinal tongue sections were captured using the Nikon AX/AX R Confocal Microscope System (Nikon), and reconstructed images were displayed by maximum intensity projection using the Nikon NIS-Elements platform (Nikon). For denervation assessment, we analyzed 100–150 NMJs located in the digastric muscles. The numbers of completely denervated (less than 10% overlapping between pre and postsynaptic terminals), partially denervated (more than 10% but less than 90% overlapping between pre and postsynaptic terminals), and innervated (more than 90% overlapping between pre and postsynaptic terminals), NMJs were counted. Note that additional materials and detailed methods of fabrication of the device (with Supplementary Note 4, Fig. S12–S14), the process of converting raw EMG data into muscle activity, finite element analysis of the system, information about animals, EMG signal monitoring in rat model, muscle tissue preparation, and statistical analysis are provided in Supplementary Information.

Reporting summary

Further information on research design is available in the Nature Portfolio Reporting Summary linked to this article.

Data availability

All data supporting the findings of this study are available within the article and its supplementary files. Source data are provided as a Source Data file, and have also been deposited in Figshare under accession code <https://doi.org/10.6084/m9.figshare.26333086.v1>. Any additional requests for information can be directed to, and will be fulfilled by, the corresponding authors. Source data are provided with this paper.

References

1. Raymond, J., Oskarsson, B., Mehta, P. & Horton, K. Clinical characteristics of a large cohort of US participants enrolled in the National Amyotrophic Lateral Sclerosis (ALS) Registry, 2010–2015. *Amyotroph. Lateral Scler. Frontotemporal Degeneration* **20**, 413–420 (2019).
2. Zarei, S. et al. A comprehensive review of amyotrophic lateral sclerosis. *Surgical Neurol. Int.* **6**, 171 (2015).
3. Tapia, R. Cellular and molecular mechanisms of motor neuron death in amyotrophic lateral sclerosis: a perspective. *Front. Cell. Neurosci.* **8**, 1–3 (2014).
4. Haverkamp, L. J., Appel, V. & Appel, S. H. Natural history of amyotrophic lateral sclerosis in a database population Validation of a scoring system and a model for survival prediction. *Brain* **118**, 707–719 (1995).
5. Armon, C. & Moses, D. Linear estimates of rates of disease progression as predictors of survival in patients with ALS entering clinical trials. *J. Neurol. Sci.* **160**, S37–S41 (1998).

6. del Aguila, M. A., Longstreth, W. T. Jr., McGuire, V., Koepsell, T. D. & van Belle, G. Prognosis in amyotrophic lateral sclerosis: a population-based study. *Neurology* **60**, 813–819 (2003).
7. Ramamoorthy, D. et al. Identifying patterns in amyotrophic lateral sclerosis progression from sparse longitudinal data. *Nat. Comput. Sci.* **2**, 605–616 (2022).
8. Aebischer, P. & Kato, A. C. Playing defense against Lou Gehrig's disease. *Sci. Am.* **297**, 86–93 (2007).
9. Rothstein, J. D. Edaravone: a new drug approved for ALS. *Cell* **171**, 725 (2017).
10. Cho, H. & Shukla, S. Role of edaravone as a treatment option for patients with amyotrophic lateral sclerosis. *Pharmaceuticals* **14**, 29 (2020).
11. Lever, T. E. et al. An animal model of oral dysphagia in amyotrophic lateral sclerosis. *Dysphagia* **24**, 180–195 (2009).
12. Malaspina, A., Jokic, N., Huang, W. L. & Priestley, J. V. Comparative analysis of the time-dependent functional and molecular changes in spinal cord degeneration induced by the G93A SOD1 gene mutation and by mechanical compression. *BMC Genomics* **9**, 500 (2008).
13. Howland, D. S. et al. Focal loss of the glutamate transporter EAAT2 in a transgenic rat model of SOD1 mutant-mediated amyotrophic lateral sclerosis (ALS). *Proc. Natl Acad. Sci.* **99**, 1604–1609 (2002).
14. Allodi, I., Montañana-Rosell, R., Selvan, R., Löw, P. & Kiehn, O. Locomotor deficits in a mouse model of ALS are paralleled by loss of V1-interneuron connections onto fast motor neurons. *Nat. Commun.* **12**, 3251 (2021).
15. Chen, X., Sanchez, G. N., Schnitzer, M. J. & Delp, S. L. Microendoscopy detects altered muscular contractile dynamics in a mouse model of amyotrophic lateral sclerosis. *Sci. Rep.* **10**, 457 (2020).
16. Hadzipasic, M. et al. Reduced high-frequency motor neuron firing, EMG fractionation, and gait variability in awake walking ALS mice. *Proc. Natl. Acad. Sci.* **113**, E7600–E7609 (2016).
17. Kühnlein, P. et al. Diagnosis and treatment of bulbar symptoms in amyotrophic lateral sclerosis. *Nat. Clin. Pract. Neurol.* **4**, 366–374 (2008).
18. McLeod, V. M. et al. Dysregulation of steroid hormone receptors in motor neurons and glia associates with disease progression in ALS mice. *Endocrinology* **161**, 1–20 (2020).
19. Shimizu, M. et al. RGMa collapses the neuronal actin barrier against disease-implicated protein and exacerbates ALS. *Sci. Adv.* **9**, eadg3193 (2023).
20. Gould, T. W. et al. Complete dissociation of motor neuron death from motor dysfunction by bax deletion in a mouse model of ALS. *J. Neurosci.* **26**, 8774–8786 (2006).
21. Aoki, M. et al. Feasibility study for functional test battery of SOD transgenic rat (H46R) and evaluation of edaravone, a free radical scavenger. *Brain Res.* **1382**, 321–325 (2011).
22. Ito, H. et al. Treatment with edaravone, initiated at symptom onset, slows motor decline and decreases SOD1 deposition in ALS mice. *Exp. Neurol.* **213**, 448–455 (2008).
23. Ikeda, K. & Iwasaki, Y. Edaravone, a free radical scavenger, delayed symptomatic and pathological progression of motor neuron disease in the wobbler mouse. *PLOS ONE* **10**, e0140316 (2015).
24. Osman, K. L. et al. Optimizing the translational value of mouse models of ALS for dysphagia therapeutic discovery. *Dysphagia* **35**, 343–359 (2020).
25. Xu, K. et al. Highly stable kirigami-structured stretchable strain sensors for perdurable wearable electronics. *J. Mater. Chem. C* **7**, 9609–9617 (2019).
26. Zhou, X. et al. All 3D-printed stretchable piezoelectric nanogenerator with non-protruding kirigami structure. *Nano Energy* **72**, 104676 (2020).
27. Brooks, A. K., Chakravarty, S., Ali, M. & Yadavalli, V. K. Kirigami-Inspired Biodesign for Applications in Healthcare. *Adv. Mater.* **34**, 2109550 (2022).
28. Rodeheaver, N. et al. Strain-isolating materials and interfacial physics for soft wearable bioelectronics and wireless, motion artifact-controlled health monitoring. *Adv. Funct. Mater.* **31**, 2104070 (2021).
29. De Luca, C. J., Donald Gilmore, L., Kuznetsov, M. & Roy, S. H. Filtering the surface EMG signal: Movement artifact and baseline noise contamination. *J. Biomech.* **43**, 1573–1579 (2010).
30. Kim, H. et al. Real-time functional assay of volumetric muscle loss injured mouse masseter muscles via nanomembrane electronics. *Adv. Sci.* **8**, 2101037 (2021).
31. Rafsanjani, A. & Bertoldi, K. Buckling-induced kirigami. *Phys. Rev. Lett.* **118**, 084301 (2017).
32. Haque, A. B. M. T., Hwang, D. & Bartlett, M. D. Graded Kirigami Composites for Programmed Strain Distributions. *Adv. Mater. Technol.* **7**, 2101241 (2022).
33. Tarasovs, S. & Andersons, J. Competition between the buckling-driven delamination and wrinkling in compressed thin coatings. *Microelectron. Reliab.* **52**, 296–299 (2012).
34. Haixia, M., Yaoyu, P., Se Hyuk, I. & Rui H. In *2008 11th Intersociety Conference on Thermal and Thermomechanical Phenomena in Electronic Systems*. pp. 762–769 (2008).
35. Blaber, J., Adair, B. & Antoniou, A. Ncorr: Open-Source 2D Digital Image Correlation Matlab Software. *Exp. Mech.* **55**, 1105–1122 (2015).
36. Liu, L. et al. Silicone-based adhesives for long-term skin application: Cleaning protocols and their effect on peel strength. *Biomed. Phys. Eng. Express* **4**, 015004 (2017).
37. Ma, D. et al. Effects of tongue force training on bulbar motor function in the female SOD1-G93A rat model of amyotrophic lateral sclerosis. *Neurorehabilitation Neural Repair* **31**, 147–156 (2017).
38. Suzuki, M. et al. Sexual dimorphism in disease onset and progression of a rat model of ALS. *Amyotroph. Lateral Scler.* **8**, 20–25 (2007).
39. Kang, D. W. et al. Pre-clinical pharmacokinetic characterization, tissue distribution, and excretion studies of novel Edaravone oral prodrug, TEJ-1704. *Pharmaceuticals* **13**, 1406 (2021).
40. Sharma, B. et al. Acute sleep deprivation induces synaptic remodeling at the soleus muscle neuromuscular junction in rats. *Sleep* **46**, 1–13 (2022).

Acknowledgements

We acknowledge the support of the NIH grant (R21EB031535) and the grant of Imagine, Innovate, and Impact (I³) from the Emory School of Medicine, Georgia Tech, through the Georgia CTSA NIH award (UL1-TR002378). This work was partially supported by the WISH Center at Georgia Tech, and the electronic devices in this work were fabricated at the Georgia Tech Institute for Matter and Systems, a member of the National Nanotechnology Coordinated Infrastructure (NNCI), which is supported by the National Science Foundation (ECCS-2025462).

Author contributions

B.S., Y.K., W.-H.Y., and H.J.C. designed the research project; B.S., Y.K., E.K., and Y.L. conducted the device fabrication and characterization; B.S., Y.K., H.K., M.M., and X.X. performed the animal study; J.L. drew illustration; B.S., Y.K., M.M., W.-H.Y., and H.J.C. analyzed data; and B.S., Y.K., W.-H.Y., and H.J.C. wrote the paper.

Competing interests

Georgia Tech has a pending US patent application regarding the materials in this paper. The remaining authors declare no competing interests.

Additional information

Supplementary information The online version contains supplementary material available at <https://doi.org/10.1038/s41467-024-51300-1>.

Correspondence and requests for materials should be addressed to Woon-Hong Yeo or Hyojung J. Choo.

Peer review information *Nature Communications* thanks Kaichen Xu, and the other, anonymous, reviewer(s) for their contribution to the peer review of this work. A peer review file is available.

Reprints and permissions information is available at <http://www.nature.com/reprints>

Publisher's note Springer Nature remains neutral with regard to jurisdictional claims in published maps and institutional affiliations.

Open Access This article is licensed under a Creative Commons Attribution-NonCommercial-NoDerivatives 4.0 International License, which permits any non-commercial use, sharing, distribution and reproduction in any medium or format, as long as you give appropriate credit to the original author(s) and the source, provide a link to the Creative Commons licence, and indicate if you modified the licensed material. You do not have permission under this licence to share adapted material derived from this article or parts of it. The images or other third party material in this article are included in the article's Creative Commons licence, unless indicated otherwise in a credit line to the material. If material is not included in the article's Creative Commons licence and your intended use is not permitted by statutory regulation or exceeds the permitted use, you will need to obtain permission directly from the copyright holder. To view a copy of this licence, visit <http://creativecommons.org/licenses/by-nc-nd/4.0/>.

© The Author(s) 2024